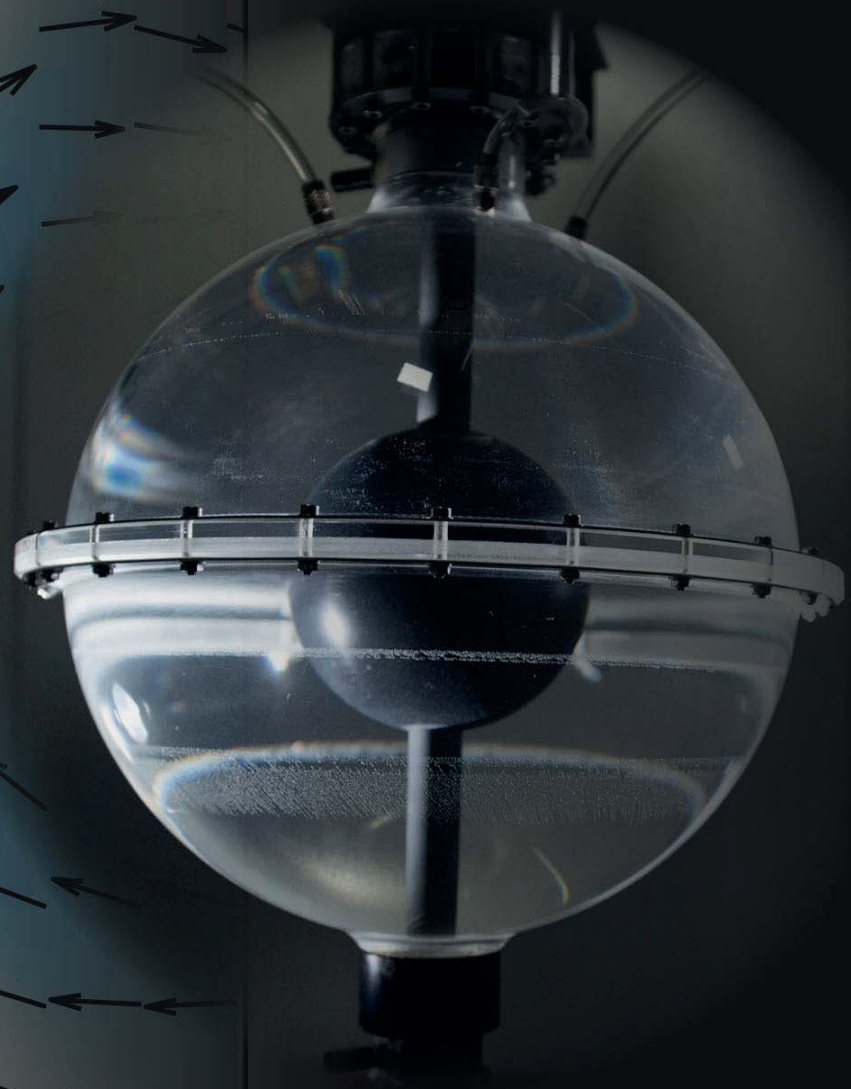


Michael Hoff

Stewartson layers, inertial waves and wave instabilities in a spherical-gap flow: Laboratory experiments with full optical access



Cuvillier Verlag Göttingen
Internationaler wissenschaftlicher Fachverlag



Stewartson layers, inertial waves and wave instabilities in a spherical-gap flow:
Laboratory experiments with full optical access



Dieses Werk ist copyrightgeschützt und darf in keiner Form vervielfältigt werden noch an Dritte weitergegeben werden.
Es gilt nur für den persönlichen Gebrauch.



Stewartson layers, inertial waves and wave instabilities in a spherical-gap flow: Laboratory experiments with full optical access

Von der Fakultät für Maschinenbau, Elektro- und Energiesysteme
– Lehrstuhl für Aerodynamik und Strömungslehre –
der Brandenburgischen Technischen Universität Cottbus–Senftenberg
zur Erlangung des akademischen Grades eines
Doktors der Ingenieurwissenschaften

genehmigte Dissertation

vorgelegt von

Master of Science (M. Sc.)
Michael HOFF

geboren am 5. Juni 1987 in Friedrichroda

Vorsitzender: Prof. Heiko Schmidt (BTU C–S)
1. Gutachter: Apl. Prof. Dr. Uwe Harlander (BTU C–S)
2. Gutachter: Prof. Dr. Christoph Egbers (BTU C–S)
3. Gutachter: Dr. Johannes Wicht (MPS Göttingen)
Tag der mündlichen Prüfung: 22. September 2017



Bibliografische Information der Deutschen Nationalbibliothek

Die Deutsche Nationalbibliothek verzeichnet diese Publikation in der Deutschen Nationalbibliographie; detaillierte bibliografische Daten sind im Internet über <http://dnb.d-nb.de> abrufbar.

1. Aufl. - Göttingen: Cuvillier, 2017

Zugl.: (TU) Cottbus, Univ., Diss., 2017

© CUVILLIER VERLAG, Göttingen 2017

Nonnenstieg 8, 37075 Göttingen

Telefon: 0551-54724-0

Telefax: 0551-54724-21

www.cuvillier.de

Alle Rechte vorbehalten. Ohne ausdrückliche Genehmigung des Verlages ist es nicht gestattet, das Buch oder Teile daraus auf fotomechanischem Weg (Fotokopie, Mikrokopie) zu vervielfältigen.

1. Auflage, 2017

Gedruckt auf umweltfreundlichem, säurefreiem Papier aus nachhaltiger Forstwirtschaft.

ISBN 978-3-7369-9644-1

eISBN 978-3-7369-8644-2

Abstract

Faculty 3 Mechanical Engineering, Electrical and Energy Systems

Department of Aerodynamics and Fluid Mechanics

Doctor of Engineering

Stewartson layers, inertial waves and wave instabilities in a spherical-gap flow: Laboratory experiments with full optical access

by Michael HOFF

We experimentally study linear and nonlinear inertial waves and modes as well as Stewartson layers in a spherical gap with a radius ratio of $\eta = r_i/r_o = 1/3$. Inertial waves and wave modes are Coriolis-restored linear waves which often arise in rapidly rotating fluids. To excite and investigate these features, two forcing systems are considered: (i) inner-sphere libration for which the sphere globally rotates at Ω_0 around its vertical axis, and a time-periodic variation of the inner sphere's angular speed in the interval $0 < \omega_{\text{lib}} < 2\Omega_0$ is overlaid, and (ii) steady differential rotation for which the inner sphere and the outer shell rotate at different speeds (spherical Couette flow), i.e. $\Omega_i \neq \Omega_o$ with $\Omega_o \neq 0$. To visualise and measure the flow, two methods based on a laser-light-sheet technique have been used: (i) qualitative measurements in the meridional plane using Kalliroscope tracer particles, and (ii) quantitative co-rotating particle-image-velocimetry (PIV) measurements in the horizontal plane using spherical tracer particles.

In the first part, we discuss the structure of the Stewartson layer in both systems. The Stewartson layer is a vertical shear layer tangential to the inner sphere's equator. For a critical shear, it becomes unstable due to shear instability. These instabilities are characterised by low-frequency wavy structures that correspond to Rossby wave instabilities. Some of these are travelling retrograde and are trapped near the Stewartson layer, others are travelling prograde filling the whole gap outside of the Stewartson layer. Since libration can be seen as a time periodic variation of differential rotation, we found the flow behaviour to be similar in both systems. The experimental results confirm theoretical, numerical, as well as other experimental studies on Stewartson-layer instabilities.

In the second part, we investigate plane inertial waves. The influence of the libration amplitude and the libration frequency on the waves and further the efficiency of the forcing to excite inertial waves are discussed. A simple 2D ray-tracing model is applied for the meridional plane to interpret the visualisations with respect to energy focusing and wave attractors. Further, nonlinear wave interactions with Rossby waves are examined.

In the third part, we investigate inertial modes in the spherical Couette flow. Recent experimental work has shown that inertial modes exist in a spherical Couette flow for $\Omega_i < \Omega_o$. A finite number of particular inertial modes has previously been found. By scanning the Rossby number from $-2.5 < Ro = (\Omega_i - \Omega_o)/\Omega_o < 0$ at two fixed Ω_o , we report the existence of similar inertial modes. However, the behaviour of the flow described here differs much from previous spherical Couette experiments. We show that the kinetic energy of the dominant inertial mode dramatically increases with decreasing Rossby number that eventually leads to a wave-breaking and an increase of small-scale structures at a critical Rossby number. Such a transition in a spherical Couette flow has not been described before. The critical Rossby number scales with the Ekman number, $E = \nu/(\Omega_o d^2)$, as $E^{1/5}$. Here, ν is the kinematic viscosity and d the gap width. Additionally, the increase of small-scale features beyond the transition transfers energy to a massively enhanced mean flow around the tangent cylinder. In this context, we discuss an interaction between the dominant inertial modes with a geostrophic Rossby mode exciting secondary modes whose frequencies match the triadic resonance condition. Results of preliminary numerical simulations confirm the experimental results.

Zusammenfassung

Fakultät 3 Maschinenbau, Elektro- und Energiesysteme

Lehrstuhl für Aerodynamik und Strömungslehre

Doktor der Ingenieurwissenschaften

Stewartsonscherschichten, Trägheitswellen und Welleninstabilitäten in einer Kugelpaltströmung: Laborexperimente mit vollem optischen Zugang

von Michael HOFF

In der vorliegenden Arbeit werden lineare und nichtlineare Trägheitswellen und Wellenmoden sowie Stewartsonscherschichten in einem konzentrischen Kugelpalt mit einem Radienverhältnis von $\eta = r_i/r_o = 1/3$ experimentell untersucht. Trägheitswellen und Trägheitsmoden sind Oszillationen, die aufgrund des Wechselspiels zwischen Corioliskraft und der Trägheit entstehen und daher häufig in schnell rotierenden Fluiden auftreten. Um diese anzuregen und zu erforschen, wird von zwei Mechanismen Gebrauch gemacht. Zum einen wird Innenkugellibration untersucht, bei welcher die gesamte Kugelschale mit einer Geschwindigkeit Ω_0 um ihre vertikale Achse rotiert und zusätzlich zur Innenkugelrotation eine periodische Oszillation im Frequenzintervall $0 < \omega_{lib} < 2\Omega_0$ auferlegt wird. Zum anderen wird stetige differentielle Rotation untersucht, bei welcher die Innenkugel- und Außenkugelrotation unterschiedlich sind, das heißt $\Omega_i \neq \Omega_o$ mit $\Omega_o \neq 0$. Eine solche Strömung wird auch sphärische Couetteströmung genannt. Um die Strömung im Kugelpalt zu visualisieren und zu messen, werden zwei Messmethoden verwendet, die auf der Laserlichtschnitttechnik basieren. In der Meridionalebene findet eine qualitative Methode Anwendung, bei der die Strömung mit sogenannten Kalliroscopepartikeln versehen wird, welche das Laserlicht in Abhängigkeit der Scherung reflektieren. In der Horizontalebene findet eine quantitative Methode, die sogenannte particle image velocimetry (PIV), Anwendung. Hierbei wird die Strömung mit sphärischen Partikeln versehen, welche das Laserlicht nahezu isotrop streuen. Gemessen wird im mitrotierenden System, sodass reine Strömungsstrukturen, die von der Festkörperrotation abweichen, untersucht werden können.

Im ersten Teil der Arbeit wird die Struktur der Stewartsonsschicht für beide Systeme untersucht. In einem Kugelpalt hat diese die Form eines vertikalen Zylinders, welcher tangential am Äquator der Innenkugel anliegt. Nachdem eine kritische Scherung überschritten ist, wird diese Schicht aufgrund von Scherinstabilitäten instabil. Diese Instabilitäten sind durch niedrigfrequente wellenartige Strukturen gekennzeichnet, die auch als Rossbywellen identifiziert werden. Einige dieser Wellen propagieren retrograd, d.h. entgegen der Rotation der Außenkugel,

und sind "gefangen" in der Scherschicht. Andere wiederum propagieren prograd, d.h. mit der Rotation der Außenkugel, und besitzen die Form von spiralförmigen Wellen, welche die gesamte Kugelspaltfläche außerhalb der Stewartsonschicht ausfüllen. Aufgrund der Tatsache, dass Libration als zeitperiodische Variation der differentiellen Rotation angesehen werden kann, weisen die Instabilitäten in beiden Systemen ein ähnliches Verhalten auf. Die aus den Experimenten erhaltenen Ergebnisse decken sich mit bisherigen numerischen und experimentellen Untersuchungen zur Stewartsonschicht.

Im zweiten Teil werden ebene Trägheitswellen untersucht. Der Einfluss der Librationsfrequenz und -amplitude auf die Wellen und die Effizienz dieser Parameter diese anzuregen, werden diskutiert. Ein einfaches zweidimensionales Raytracingmodel wird auf die Meridionalebene angewendet, um die experimentellen Befunde im Bezug auf Energiefokussierung und Wellenatraktoren zu interpretieren. Abschließend werden nichtlineare Interaktionen zwischen ebenen Trägheitswellen und Rossbywellen identifiziert und diskutiert.

Im dritten Teil werden Trägheitsmoden in der sphärischen Couetteströmung untersucht. Neueste experimentelle Arbeiten haben gezeigt, dass eine finite Anzahl solcher Moden in der sphärischen Couetteströmung existiert, wenn $\Omega_i < \Omega_o$ gilt. Für zwei festgelegte Ω_o wurden experimentelle "Rampen" durchgeführt, bei welchen die charakteristische Rossbyzahl in einem Intervall $-2.5 < Ro = (\Omega_i - \Omega_o)/\Omega_o < 0$ mit ausreichend kleinen Schritten abgetastet wurde. Die experimentellen Befunden weisen die Existenz ähnlicher Trägheitsmoden auf. Allerdings ist das Strömungsverhalten im kompletten Intervall grundsätzlich unterschiedlich im Vergleich zu bisher untersuchten sphärischen Couetteströmungen. Es wird gezeigt, dass die kinetische Energie der dominanten Trägheitsmode mit abnehmender Rossbyzahl dramatisch ansteigt. Dies führt letztendlich zu einer Art "Wellenbrechen" ab einer kritischen Rossbyzahl, bei dem ein signifikanter Anstieg kleinskaliger Strukturen zu verzeichnen ist. Diese kritische Rossbyzahl skaliert mit der Ekmanzahl, $E = \nu/(\Omega_o d^2)$, mit einer Potenz von $E^{1/5}$. Hierbei ist ν die kinematische Viskosität des Fluids und d ist die Spaltweite. Zusätzlich bewirkt der Anstieg kleinskaliger Turbulenz einen Energietransfer zu einem massiv verstärkten Grundstrom nahe des Tangentzyinders. In diesem Zusammenhang werden nichtlineare Wechselwirkungen zwischen Trägheitsmoden und einer sehr dominanten Rossbymode mit der azimuthalen Wellenzahl $m = 1$ untersucht. Diese führen zu einer triadischen Resonanz, bei welcher sekundäre Wellenmoden erzeugt werden, dessen Frequenz der Summe oder Differenz der primären Wellen entspricht. Abschließend werden vorläufige numerische Ergebnisse zur Bestätigung der experimentellen Ergebnisse aufgezeigt.



Contents

Abstract	iii
Zusammenfassung	v
Contents	vii
List of Figures	xi
List of Tables	xv
Abbreviations	xvii
1 Introduction	1
1.1 Why spherical-gap geometry?	1
1.2 About this thesis	5
2 Fundamentals	11
2.1 Equations of motion	11
2.1.1 Pressure gradient acceleration	12
2.1.2 Gravitational acceleration	12
2.1.3 Friction acceleration	12
2.1.4 Apparent accelerations	13
2.1.5 The Navier-Stokes equation	15
2.2 The continuity equation	15
2.3 Plane inertial waves in unbounded fluids	16
2.3.1 The dispersion relationship	17
2.3.2 Phase- and group velocity	20
2.3.3 Limiting case of a high-frequency wave	21
2.3.4 Limiting case of a low-frequency wave	21
2.4 Inertial waves in bounded fluids	23
2.4.1 Reflection of inertial waves at inclined boundaries	23
2.4.2 Wave rays, closed orbits and attractors	25
2.5 Inertial waves in spheres and spherical gaps	27
2.5.1 Inertial modes in a sphere	27
2.5.2 Inertial waves in a spherical gap - shear layers	34

2.6	Taylor-Proudman theorem	36
2.7	Over-reflection and Critical layers	37
3	Experimental setup	39
3.1	Description of the apparatus	40
3.2	Control unit	42
3.3	Libration efficiency	43
3.4	Calibration of rotation rate and libration	45
3.4.1	Setup and method	45
3.4.2	Calibration of the outer and inner sphere	47
3.4.3	Calibration of the libration parameters	48
3.4.4	Calibration of the differential rotation	50
4	Measurement techniques	53
4.1	Laser-light-sheet technique	54
4.2	Qualitative measurements in the meridional plane	56
4.3	Quantitative measurements in the horizontal plane (planar PIV)	57
4.3.1	General overview and fundamentals	58
4.3.2	Setup and experimental procedure	61
4.3.3	The GoPro camera and its properties	62
4.3.4	The MatPIV toolbox and its application to the data	64
4.3.5	Error estimation	66
5	Post-processing methods	69
5.1	Discrete Fourier transformation	69
5.2	Harmonic analysis	69
5.2.1	Least-square method	71
5.2.2	General form of the matrix equation	71
5.2.3	Example with one dominant frequency	72
5.3	Bispectral analysis - Bicoherence	74
5.4	EOF and CEOF analysis	77
5.5	Estimation of the linear propagator	80
5.6	Estimation of principle oscillation patterns (POPs)	83
5.7	Estimation of singular vectors (SVs)	83
5.8	Relationship between SVs, POPs and adjoint POPs	84
6	The Stewartson layer	87
6.1	About Stewartson layers and their instabilities	87
6.1.1	What is the Stewartson layer?	87
6.1.2	Instabilities of the Stewartson layer	92
6.2	The classical Stewartson layer with differentially rotating boundaries	95
6.2.1	Data and data processing	95
6.2.2	The structure of the Stewartson layer	97
6.2.3	Route to Stewartson-layer instability for increasing $ Ro $	101
6.2.4	The scaling-law of the Stewartson-layer instability	103
6.2.5	Patterns of Stewartson-layer instability for $Ro < 0$ and $Ro > 0$	105
6.2.6	Interactions between mean flow and spiral waves	108
6.3	The ‘new’ jet-like Stewartson layer for inner-sphere libration	110

6.3.1	Data and data processing	110
6.3.2	The Structure of the Stewartson layer	113
6.3.3	Route to Stewartson-layer instability for high $\hat{\epsilon}_{\text{lib}}$ and small $\hat{\omega}_{\text{lib}}$	116
6.3.4	Patterns of Stewartson-layer instability for librating inner sphere	119
6.4	Discussion and comparison	123
7	Linear inertial waves driven by inner sphere libration	129
7.1	Introduction	130
7.2	The ray-tracing model	131
7.3	Data and data processing	134
7.4	Linear inertial waves in the meridional plane	135
7.5	Linear inertial waves in the horizontal plane	139
7.6	Triad interactions with Rossby waves	141
7.7	Summary and conclusion	144
8	Inertial modes driven by differential rotation	145
8.1	Introduction	146
8.2	Experimental setup and data processing	148
8.2.1	Experimental setup	148
8.2.2	Data and data processing	150
8.3	The velocity spectrograms	151
8.4	Inertial wave modes' detection and comparison with the literature	154
8.5	The excitation of inertial modes – the presence of critical layers?	159
8.6	Transition to small-scale turbulence	160
8.6.1	Kinetic energy distribution - mode amplification and zonal mean flow enhancement	161
8.6.2	Frequency shift of the dominant wave modes – Doppler effect	162
8.6.3	The scaling-law of Ro_c	165
8.6.4	Increased turbulence in the inertial wave range	167
8.6.5	Subharmonic instability as an explanation for the transition to wave turbulence?	168
8.6.6	Non-modal growth as an explanation for the transition to wave turbulence?	169
8.7	Preliminary results of accompanying numerical simulations	173
8.8	Discussion and conclusion	178
9	Concluding remarks	185
A	Ray-tracing - detecting the correct intersection point	193
A.1	Whole spherical gap without the shaft	193
A.2	Half spherical gap including the shaft	195
B	Correction of radial distortion	197
C	Inertial mode spectrograms in the meridional plane	201
Bibliography		203
Acknowledgements		215



Dieses Werk ist copyrightgeschützt und darf in keiner Form vervielfältigt werden noch an Dritte weitergegeben werden.
Es gilt nur für den persönlichen Gebrauch.

List of Figures

1.1	Image of the Earth and its different layers.	1
1.2	Flow chart illustrating the two different rotational systems investigated in this thesis.	6
2.1	Sketch of the evolution of an inertial oscillation of a fluid particle restored by the Coriolis force.	17
2.2	Schematic view of an inertial wave with a certain frequency ω according to the dispersion relationship (Messio <i>et al.</i> , 2008).	19
2.3	Schematic view of the inertial wave properties, i.e. wave vector, velocity, phase velocity and group velocity for high and low frequencies (Messio <i>et al.</i> , 2008).	22
2.4	Reflection law of inertial waves (Manders, 2003).	24
2.5	The four possible directions of wave characteristics for a certain frequency ω (Borcia and Harlander, 2013).	26
2.6	Sketch of a wave attractor in a rotating container with one sloping wall and a corresponding experimental result (Maas, 2001).	26
2.7	3D visualisations of two eigenmodes in the full sphere. The plots are provide by A. Barik (MPS).	29
2.8	(a) Circulation patterns for the axially symmetric low-order spherical modes with $(l, m = 0, n)$ (Greenspan, 1968). (b) Amplitude response of the sphere, measured from a pressure probe. Modes got excited by librations of the sphere (Aldridge, 1967, Aldridge and Toomre, 1969).	31
2.9	A diagram of the viscous response to a spin-over velocity field ($\hat{\omega} = 1$) in a spherical gap (Kerswell, 1995).	35
3.1	Image and sketch of the spehrical-gap apparatus	40
3.2	LabVIEW® graphical user interface.	43
3.3	Graphical illustration of the inner sphere excursion as a function of $\hat{\omega}_{\text{lib}}$ and $\hat{\epsilon}_{\text{lib}}$	44
3.4	Sketch of calibration measurement method.	46
3.5	Image of calibration measurement and post-processing	46
3.6	Time series of the marker after calibration.	48
4.1	Schematic drawing of the laser-light sheet setup in the spherical gap.	55
4.2	Image of the Linos Nano 250-532-100 laser.	55
4.3	Example images of qualitative measurements in the meridional plane.	57
4.4	Principle of planar PIV (Raffel, 2007).	58
4.5	Two examples of sub-windows of a particle visualisation and a corresponding cross-correlation map (Sveen and Cowen, 2004).	60
4.6	Experimental setup for PIV measurements in the spherical gap in the co-rotating frame.	61

4.7	The GoPro Hero 3+ black edition camera with and without waterproof housing and its remote control. Source: www.chip.de	62
4.8	Illustration of a radial distortion and its correction (Hartley and Zisserman, 2003).	63
4.9	Setup for the record of the coordinate system for PIV analysis.	65
4.10	Image of the coordinate system as it was used for calibration of PIV.	66
4.11	A series of schematic images including the ‘rotating’ shaft.	68
5.1	Left: Symmetry regions of third-order moments. Right: Symmetry regions of a bispectrum (Nagata, 1978).	76
6.1	Sketches of the Stewartson layer and its scaling laws (Stewartson, 1966)	88
6.2	Graphical illustration of the velocity profiles in a differentially rotating spherical gap.	88
6.3	Sketch of the time-averaged azimuthal velocity in a spherical gap, where the inner sphere librates.	91
6.4	Sketches of the Stewartson-layer instabilities taken from Schaeffer and Cardin (2005a).	93
6.5	β parameter in a spherical gap as a function of radius.	94
6.6	Graphical illustration of the experimental parameters for the Stewartson-layer instabilities.	96
6.7	Kalliroscope visualisations in the meridional plane for $\Omega_o = 42.5$ r.p.m. for $Ro > 0$ and $Ro < 0$	97
6.8	Azimuthally and time-averaged radial profile of the azimuthal velocity in mm s^{-1} (left) for $\Omega_o = 30$ r.p.m. and $Ro \approx -0.1$ and the corresponding relative vorticity profile (right).	98
6.9	Azimuthally averaged radial profiles of the azimuthal mean flow for different Ekman numbers for $Ro \approx \pm 0.1$ (left) and $Ro \approx \pm 0.29$ (right).	99
6.10	Azimuthally averaged azimuthal mean flow as a function of the Rossby number for $\Omega_o = 32$ r.p.m., $E = 3.04 \cdot 10^{-5}$ (upper panel) and for $\Omega_o = 64$ r.p.m., $E = 1.52 \cdot 10^{-5}$ (lower panel).	100
6.11	Azimuthal-velocity spectrograms showing the Stewartson-layer instabilities for $\Omega_o \approx 32$ r.p.m. and $\Omega_o \approx 64$ r.p.m..	101
6.12	Onsets of Stewartson-layer instabilities as a function of Ekman number.	104
6.13	Stewartson-layer instability patterns at $h = 4$ cm for sub-rotation, $Ro = -0.33$, and $\Omega_o \approx 64$ r.p.m./ $E = 1.52 \cdot 10^{-5}$	106
6.14	Stewartson-layer instability patterns at $h = 4$ cm for super-rotation, $Ro > 0$, and $\Omega_o \approx 32$ r.p.m./ $E = 3.04 \cdot 10^{-5}$	107
6.15	A series of five reconstructed spiral patterns taken from the $m = 4$ branch in Fig. 6.11(b) for super-rotation.	109
6.16	Azimuthal velocity in mm s^{-1} (blue axis) and the wave frequency, $\hat{\omega}$ (green axis), as a function of the Rossby number, Ro	110
6.17	Regime diagram for inner sphere libration and representative Kalliroscope visualisations.	112
6.18	Kalliroscope visualisations in the meridional plane averaged over two minutes, depending on the libration parameters, $\hat{\omega}_{\text{lib}}$ and $\hat{\epsilon}_{\text{lib}}$	114
6.19	Results of the mean flow induced by inner sphere libration (horizontal, $\hat{\omega}_{\text{lib}}$ -dependency and $\hat{\epsilon}_{\text{lib}}$ -dependency)	115
6.20	Single-sided amplitude spectra taken from a Fourier analysis for different libration frequencies and mean rotation rates.	118

6.21	Velocity fields of the trapped Rossby waves for inner sphere libration.	120
6.22	Velocity fields of the spiral Rossby waves for inner sphere libration.	122
6.23	Flow chart illustrating all detected Stewartson-layer instabilities and their wavenumber dependencies on the Ekman number and frequency.	125
7.1	Sketch of inertial-wave characteristics with $\hat{\omega}_{\text{lib}} = 0.4$ as the excitation frequency and three possible higher harmonics with $k\hat{\omega}_{\text{lib}}$, $k = 2, 3, 4$, for $\eta = 1/3$	131
7.2	Identical to Fig. 6.17. Regime diagram for inner sphere libration.	134
7.3	Ray paths for three different frequencies.	135
7.4	Poincare plot for $\eta = 1/3$ starting at ϑ_c pointing northward	136
7.5	Phases of the inertial waves for different $\hat{\omega}_{\text{lib}}$ computed via a harmonic analysis	137
7.6	Comparison between measured inertial waves and ray-tracing in the meridional plane.	138
7.7	Wave amplitude $(\overline{u_\phi^2}^{\phi,t})^{1/2}$ for different libration frequencies filtered by a harmonic analysis.	139
7.8	Horizontal velocity fields for $h = 2$ cm (a,b) and $h = 4$ cm (c,d) filtered for the libration frequency, $\hat{\omega}_{\text{lib}} = 0.4$, with the help of a harmonic analysis.	140
7.9	Bicoherence spectra in the supercritical regime, computed via (5.30). The libration parameters are $\hat{\omega}_{\text{lib}} = 0.6$ and $\hat{\epsilon}_{\text{lib}} = 1.0$	143
8.1	Sketch of the spherical-gap setup.	149
8.2	Graphical illustration of the experimental parameters for the inertial mode analysis.	150
8.3	Azimuthal-velocity spectrogram showing the inertial modes for $\Omega_o \approx 32$ r.p.m. and $E = 3.04 \cdot 10^{-5}$	152
8.4	Azimuthal-velocity spectrogram showing the inertial modes for $\Omega_o \approx 64$ r.p.m. and $E = 1.52 \cdot 10^{-5}$	152
8.5	Temporal and azimuthal average of the azimuthal velocity $(\overline{v_\phi^t}^{\phi})$ in mm s^{-1} as a function of radius and Rossby number, $Ro < 0$	155
8.6	Comparison between measured inertial modes in the spherical gap and analytic inertial modes in the full sphere.	157
8.7	Maximum kinetic energy of the (3,2) and (5,1) mode and lower sideband as a function of the Rossby number for $\Omega_o \approx 32$ r.p.m. and $E = 3.04 \cdot 10^{-5}$ (left) and $\Omega_o \approx 64$ r.p.m. and $E = 1.52 \cdot 10^{-5}$ (right).	161
8.8	Two amplitude spectra $ X(\hat{\omega}) /n$ extracted from Fig. 8.4 for $Ro = -1.76$ (black) in the weakly-turbulent regime (III) and $Ro = -1.73$ (red) in the strong-inertial-mode regime (II).	163
8.9	Critical Rossby number Ro_c (crosses) where the weak turbulence (III) transitions into a strong-inertial-mode regime (II) as a function of the Ekman number.	165
8.10	Snapshots of measurements in the meridional plane using a vertical laser light sheet. The left image has been taken in the weakly-turbulent regime (III) and the right image in the strong-inertial-mode regime (II).	167
8.11	Two amplitude spectra $ X(\hat{\omega}) /n$ in log-log scale extracted from Fig. 8.4 for $Ro = -1.82$ (red) in the weakly-turbulent regime (III) and $Ro = -1.68$ (black) in the strong-inertial-mode regime (II).	168
8.12	Bicoherence calculated for $E = 1.52 \cdot 10^{-5}$ and $Ro \approx -1.73$ (top) in regime (II) and $Ro \approx -1.82$ (bottom) in regime (III) for the same spatial region as the spectrogram in Fig. 8.4.	170

8.13 POP analysis of a representative data set in the strong-inertial-mode regime (II) and the weakly-turbulent regime (III).	172
8.14 Numerical spectrogram for $E = 1.125 \cdot 10^{-4}$, created from XHELLS. Plot is provided by S. A. Triana.	175
8.15 Comparison between experimentally ($E = 1.52 \cdot 10^{-5}$) (left) and numerically ($E = 10^{-5}$) (MagIC) (right) obtained inertial modes in a horizontal plane, $h = 4$ cm above the equator. Numerical plots are provided by A. Barik.	176
8.16 Numerical bicoherence spectrum for $E = 10^{-4}$ and $Ro = -2.0$ (regime II), using MagIC. Plot is provided by A. Barik.	177
8.17 Numerically obtained instantaneous velocity for $E = 10^{-4}$ as a function of Ro and cylindrical radius s/r_o , using MagIC. Plot is provided by A. Barik.	178
8.18 Structural change of the numerical (3,2) mode from a top view for different Rossby numbers $ Ro $ at $E = 10^{-4}$. Plots are provided by A. Barik using MagIC code.	181
8.19 Frequency of the (6,1) eigenmode of the spherical gap (left) and the corresponding damping rate as a function of radius ratio at $E = 10^{-5}$. Plots are provided by S. A. Triana.	182
8.20 Structure of the numerical (3,2) mode in the meridional plane for different Rossby numbers $ Ro $ at $E = 10^{-4}$. Plots are provided by A. Barik using MagIC code.	182
A.1 Ray-tracing: different cases of possible intersection points between the ray and the boundaries in the full sphere without a shaft.	194
A.2 Ray-tracing: different cases of possible intersection points between the ray and the boundaries in the half sphere including the shaft.	195
B.1 Sequence of camera calibration images for GoPro Hero 3+ black edition with 1080p medium FoV.	199
B.2 Left: Mean reprojection error per image. Right: Extrinsic parameters visualisation.	199
C.1 Kalliroscope-based spectrograms for the meridional plane taken from a ramp where each inner sphere rotation was kept constant for 20 min (including 5 min spin-up time).	202

List of Tables

1.1	Examples of spherical gaps on the Earth.	2
3.1	Geometrical and experimental parameters of the spherical-gap experiment	41
3.2	Comparison between the measured excursion of the marker and the analytic excursions for $\hat{\omega}_{\text{lib}}$	49
3.3	Comparison between the measured excursion of the marker and the analytic excursions for $\hat{\epsilon}_{\text{lib}}$	50
4.1	Refraction-index adjustment for the spherical-gap experiments.	54
4.2	Specifications of the Laser Linos Nano 250-532-100.	55
6.1	Scaling laws of the first Stewartson-layer instability for the different signs of Ro as they could be found in the literature survey.	104
6.2	Appearance, amplitude and frequency of the trapped Rossby waves depending on the libration frequency.	121
8.1	Geometrical and experimental parameters of the spherical-gap experiment.	149
8.2	Uniquely identified inertial modes in regime (II), according to Fig. 8.6.	158
8.3	Frequency values of the three dominant modes before and after the transition from regime (II) to (III), the velocity difference resulting from the Doppler shift, and the measured velocity shift of the mean flow, averaged over ϕ and r	164



Dieses Werk ist copyrightgeschützt und darf in keiner Form vervielfältigt werden noch an Dritte weitergegeben werden.
Es gilt nur für den persönlichen Gebrauch.

Abbreviations

CEO	complex empirical orthogonal function
DFT	discrete Fourier transformation
EOF	empirical orthogonal function
ESV	evolved singular vector
FFT	fast Fourier transform
FoV	field of view
fps	frames per second
HOS	higher order spectra
HOSA	higher order spectral analysis
ISO	International Organization for Standardization
ISS	International Space Station
ISV	initial singular vector
LabView	Laboratory Virtual Instrument Engineering Workbench
LDA	laser Doppler anemometry
LDV	laser Doppler velocimetry
LLV	local Lyapunov vector
Matlab	Matrix Laboratory
MPS	Max Planck Institute for Solar System Research
PC	principle component
PCA	principle component analysis
PE	Poincaré equation
PIV	particle image velocimetry
POD	proper orthogonal decomposition
POP	principle oscillation pattern
QG	quasi-geostrophic



r.p.m.	rounds per minute
SL	Stewartson layer
SNR	signal-to-noise ratio
SV	singular vector
SVD	singular vector decomposition
TC	tangent cylinder

Chapter 1

Introduction

1.1 Why spherical-gap geometry?

Many planetary bodies in our solar system consist of a solid inner and a liquid outer core, surrounded by a ‘solid’ shell (the outer spherical shell). The region between two such concentric spheres is called *spherical gap*. Such fluid-filled spherical gaps are omnipresent in nature. The most obvious example is given by our Earth (Fig. 1.1). But also other planets, like Mercury, Jupiter and Saturn, as well as the Earth’s moon and the Galilean moons of Jupiter consist of spherical-gap geometry (see e.g. Spohn, 2007). In principle, the Earth consists of different layers (Fig. 1.1), so-called spherical shells, which are separated with respect to their density distribution but also to their particular dynamical and chemical processes (rotation, convection, tectonics, etc.). The solid inner core, the liquid outer core, the mantle and the crust (continental as well as oceanic) build the basis of the Earth’s structure. The atmosphere, particularly the troposphere, and the oceans represent an outer fluid layer, dominated by large and small-scale dynamical motions as well. Because of these different layers, several fields of applications of spherical gaps can be noticed (see Tab. 1.1). Assuming that the tropopause is a boundary where,

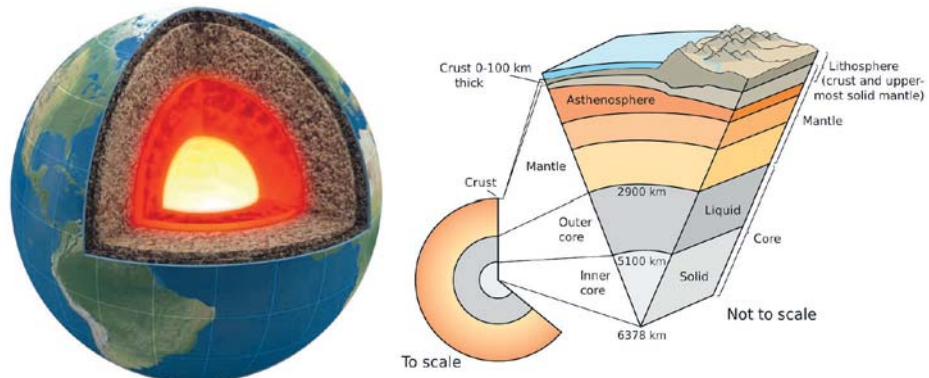


FIGURE 1.1: Image of the Earth and its different layers. Picture taken from Kious *et al.* (1996).

<i>inner sphere</i>	<i>outer shell</i>	<i>gap-filling fluid</i>	<i>relevant for</i>
continental crust	tropopause	moist air mixture	Meteorology
ocean crust	ocean surface	saline water	Oceanography
solid iron core	lower mantle	molten metal	Geophysics/ Astrophysics

TABLE 1.1: Examples of spherical gaps on the Earth.

for example, waves get reflected, the troposphere forms a very thin spherical gap, for which the continental crust forms the inner sphere. This behaves similarly for the ocean and the oceanic crust. From theoretical models of the equatorial ocean and atmospheric dynamics, there remain large uncertainties since most of the models make use of the traditional approximation that neglects the vertical component of the Coriolis force. Laboratory and numerical experiments in spherical-gap geometry are not affected by this kind of approximations and might hence form a testbed for the subtle equatorial dynamics of geophysical flows (see e.g. Harlander and Maas, 2006, 2007a, Rabitti and Maas, 2013, 2014, Rabitti, 2016). However, in terms of the radius ratio, the present work is more related to thick spherical gaps like the Earth's core. It has a radius ratio of about $r_i/r_o \approx 0.35$ (Spohn, 2007), being r_i and r_o the inner and outer sphere radius, which is close to $r_i/r_o = 1/3$ used for the present work.

The Earth's core is one of the most inaccessible places in the universe. The Kola borehole is the deepest borehole in the history of exploration of the Earth's interior. However, with a depth of ~ 12 km it just ‘scratches’ the surface, considering that the inner core begins at around 2900 km depth. In contrast, gravimetric analysis and measurements of seismic activities are indirect methods to determine, for example, the density of the inner core or its spin rate. But also volcanic activity and the structure of meteorites can be used to obtain information about the Earth's interior. Despite all these efforts, most of the structure and dynamical behaviour of the Earth's core remains uncertain and unknown. Therefore, it is indispensable to use alternatives like spherical-gap models (theoretically, numerically and experimentally) to investigate the dynamics and underlying mechanisms of the Earth's liquid outer core, and eventually extrapolate certain aspects to planetary scales with the help of scaling laws.

One particular property of spherical gaps, like planetary cores, is that they do not rotate constantly since there is additional forcing. There are three main periodic forcing mechanisms: (i) precession, which is a periodic variation of the rotation vector, (ii) tidal forcing, which is a periodic variation in shape, and (iii) longitudinal libration, which is a superposed oscillation on the rotation speed. A rather steady forcing, which is roughly related to libration, is steady differential rotation for which the inner core and outer shell rotate constantly at different speeds. Many planetary bodies and satellites, like Mercury, the Earth's moon or the Galilean moons of Jupiter librate due to interactions with their gravitational partners (see e.g. Comstock and Bills, 2003). The Earth's core, on the other hand, undergoes a slight differential rotation ($\mathcal{O}(10^{-6})$) where the inner core and outer mantle rotate at different speeds. This happens due to a strong

gravitational coupling between the mantle and the inner core where small fluctuations of the mantle momentum have a strong impact on the inner core's rotation (Aldridge and Lumb, 1987, Rieutord, 1995). One source for such fluctuations is proven to be strong earthquakes (Song and Richards, 1996, Buffett, 1997). Apart from planetary-shaped bodies, also accretion disks are driven by differential rotation (Li *et al.*, 2000, 2001) and can approximately be modelled by spherical gaps. Two review articles about fluid motions in spheres, spherical gaps and spheroids have recently been published by Le Bars *et al.* (2015) and Le Bars (2016).

All these rotational background systems have a significant influence on the fluid in the interior of planets and stars. It is worth to know the interaction between the core rotation and the interior of the fluid to understand, for example, tidal heating, fluid mixing, and the generation of magnetic fields. About the importance and the recent necessity of investigations of pure rotational effects, Le Bars *et al.* (2015) stated the following: For more than half a century most research on fluid dynamics in planetary liquid core models focused on convective processes. The main purpose of this past research was to demonstrate that convective flows in a rotating spherical gap can generate a dynamo. Most notably the magnetic field of the Earth is caused by such motions. However, it is difficult to validate these models with observational data since sufficiently high temperature gradients cannot be reached neither by laboratory experiments nor by numerical models, or, obtained standard scaling laws fail to extrapolate to real astrophysical systems. Moreover, Le Bars *et al.* (2015) noted that it is often assumed that fluid motions in astrophysical bodies are controlled and driven by convective effects only. However, in situ data from space missions of the last couple of years imply that there is a huge reservoir of energy stored in the rotational motion of planets and stars which can sustain intense large-scale flows. Therefore, studies on pure rotational effects in planetary core shaped models gain increasing attention (the reader is referred to Le Bars *et al.*, 2015, Le Bars, 2016, for more detailed information).

Moreover, they stated that the mechanical forcings, which are small compared to the overall rotation, do not directly provide the energy to drive particular flows. They act more as conveyors that extract a part of the potential rotational energy and transfer it to intense large-scale fluid motions. Such motions can be inertial waves or wave modes (e.g. in the Earth's liquid outer core, Aldridge and Lumb, 1987, Rieutord, 1995) and Stewartson shear layers (Stewartson, 1957, 1966, Hide and Titman, 1967, Früh and Read, 1999, Hollerbach, 2003, Koch *et al.*, 2013, Sauret and Le Dizès, 2013). Even more, this energy transfer gives rise to various types of instabilities (e.g. elliptical instability, shear instability or centrifugal instability) which are the topics of the present work. Of particular interest are wave interactions and Stewartson layer instabilities (Hide and Titman, 1967, Hollerbach, 2003, Hollerbach *et al.*, 2004, Schaeffer and Cardin, 2005a,b, Wicht, 2014).

An opportunity to explore aspects of the dynamics and mechanisms in planets and stars is to do laboratory experiments. Usually, planets, atmospheres and oceans are complex systems with a